Statistical Comparison of Cardiac Fibre Architectures

Jean-Marc Peyrat[1], Maxime Sermesant[1,2], Xavier Pennec[1], Hervé Delingette[1], Chenyang Xu[3], Elliot McVeigh[4], and Nicholas Ayache[1]

[1] INRIA - Asclepios Research Project, Sophia Antipolis, France
jean-marc.peyrat@sophia.inria.fr
[2] King's College London, Cardiac MR Research Group, Guy's Hospital, London, UK
[3] Siemens Corporate Research, Princeton, New Jersey, USA
[4] Laboratory of Cardiac Energetics, National Heart Lung and Blood Institute, National Institutes of Health, Bethesda, Maryland, USA

Abstract. In this paper, a statistical atlas of DT-MRIs based on a population of nine *ex vivo* normal canine hearts is compared with a human cardiac DT-MRI and a commonly used synthetic model of the fibre orientation. The aim of this paper is to perform an statistical inter-species comparison of the cardiac fibre architecture and to assess the quality of a synthetic description of the fibre orientation. First, we present the framework to build a statistical atlas of cardiac DT-MRIs providing a mean and a covariance of diffusion tensors at each voxel of an average geometry. According to the registration steps of this framework, we register the human and synthetic data on the statistical atlas. Finally, for each eigenvectors of the diffusion tensors, we compute the angular difference with the average atlas and its Mahalanobis distance to the canine population. The results show a better consistence of the fibre orientation than the laminar sheet orientation between the human and the canine heart, while the homogeneous synthetic model appears too simple compared to the complexity of real cardiac geometry and fibre architecture.

1 Introduction

The cardiac fibre architecture plays a key role in normal and pathological heart functions. For many years, the orientation of these fibres and their arrangement in laminar sheets have been studied with histological slices [13,22]. Recently, the measurements of fibre structure have been eased with diffusion tensor magnetic imaging (DT-MRI) since a correlation between the myocardium fibre architecture and diffusion tensors has been shown [10,19]. The acquisition of high resolution *in vivo* DT-MRI is a very challenging task due to cardiac motion [8]. Hence, modeling the cardiac fibre architecture [4,12,18] is essential for clinical applications such as the planning of patient-specific cardiac therapies [21]. This architecture has been included into an electromechanical model based on a single canine DT-MRI acquisition of an *ex vivo* heart [20] or a synthetic model [21] registered on the patient data. These electromechanical models are usually limited

to the cardiac fibre orientation whereas the laminar sheets have been shown to contribute to the cardiac motion [3, 7, 14, 24], especially for a better electromechanical modeling of the wall thickening and the apico-basal torsion.

We propose here to compare a statistical atlas of the complete cardiac fibre architecture of a population of nine *ex vivo* canine hearts with a human heart and a synthetic model used in [21]. The inter-species comparison of the cardiac fibre architecture is a first step to assess the relevance of a canine statistical atlas for clinical applications. A one-to-one comparison between the synthetic model and the canine hearts has already been performed [23] but the quantification of their differences was limited to the percentage of angular differences below a given threshold. We propose here to extend these studies comparing the synthetic model with a statistical atlas including an information about the variability of the population. We also study the spatial distribution of their differences to know where the synthetic model needs to be improved.

First, we present an extension of the framework for building a statistical atlas of the cardiac fibre architecture proposed in [17]. Second, we perform an inter-species comparison of the cardiac fibre architecture between a human heart and a population of canine hearts. Finally, we compare the synthetic model used for electromechanical modeling with the statistical atlas.

2 Data Acquisition

We used a DT-MRIs dataset of *ex vivo* fixed normal hearts (9 canine and 1 human) acquired [11] by the Center of Cardiovascular Bioinformatics and Modeling (CCBM) at the Johns Hopkins University and available on the internet[5]. Each heart was placed in an acrylic container filled with Fomblin, a perfluoropolyether (Ausimon, Thorofare, NJ). Fomblin has a low dielectric effect and minimal MR signal thereby increasing contrast and eliminating unwanted susceptibility artifacts near the boundaries of the heart. The long axis of the hearts were aligned with the z-axis of the scanner. Images were acquired with a 4-element knee phased array coil on a 1.5 T GE CV/i MRI Scanner (GE, Medical System, Wausheka, WI) using a gradient system (from 14 to 28 gradients) with 40 mT/m maximum gradient amplitude and a 150 $T/m/s$ slew rate. The resolution of the images are around $0.3 \times 0.3 \times 0.9$ mm^3 per voxel. The acquisition temperature was different from one heart to another in a range from 18 to 25°C.

3 Construction of the Statistical Atlas

The construction of the statistical atlas of the cardiac fibre architecture is based on a framework [17] using the Log-Euclidean metric [2]. We modified this framework providing an average cardiac geometry that includes both atria and where diffusion tensors are normalized to minimize the influence of acquisition parameters on statistics. We also preferred another reorientation strategy [1] in the diffusion tensor registration process.

[5] http://www.ccbm.jhu.edu/research/DTMRIDS.php

Pre-Processing: First, we apply a basic threshold to the DT-MRIs based on the Log-Euclidean norm [2] to segment the meaningful cardiac structures in terms of cardiac fibre architecture. While our previous work [17] was focusing on the compact myocardium of the ventricles, we extend the construction of the atlas to the atria. To avoid any influence of the dispersion of the diffusion rates that are not due to an intrinsic variability between hearts such as the temperature of acquisition, we perform a global normalization of each diffusion tensor field to equalize the average value of the histogram of the norm of diffusion tensors of each heart. The statistical analysis of the diffusion rates can still give an information about the spatial variability of diffusion rates. The resulting normalized atlas is finally scaled by the average of all these normalization factors to include realistic averaged diffusion rates.

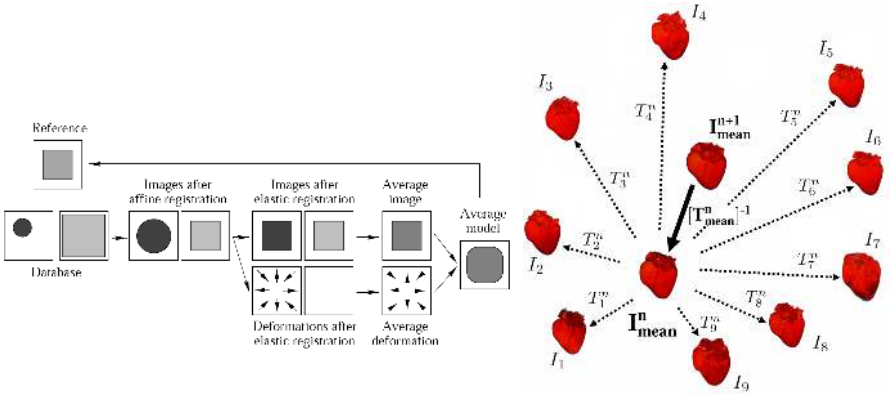

Fig. 1. [*Left*] Registration of anatomical MRIs using an iterative process averaging the intensities (light and dark grey) and the shape (circles and squares) of the dataset (from Guimond *et al.* [9]). [*Right*] The iterative registration process uses the average geometry as a reference for the next step. The deformation field T_i^n is a composition of an affine transformation S (in our case a non-uniform scaling transformation) and a non-rigid deformation.

Registration of the anatomical MRIs: The core of the registration algorithm is exactly the same as the one we already presented [17]. First, we proceed to a global registration based on a non-uniform similarity transformation defined by three manually located landmarks: the apex and the two corner points in the valve plane. Secondly, to find the residual non-rigid deformation we use a hybrid intensity- and landmark-based registration algorithm [5]. With this algorithm we can interactively select pairs of landmarks which will constrain the non-rigid intensity-based registration. This hybrid algorithm can be used with any intensity-based registration algorithm and in this case, we combine it with a diffeomorphic registration algorithm [6] based on the mutual information.

In this framework, the geometry of the average anatomical MRI is the geometry of a chosen reference heart. We propose here to add to this framework an iterative process that converges to an average geometry and intensities of

anatomical MRIs. We based this modification on the brain averaging strategy proposed by Guimond *et al.* [9]. We iteratively build an average geometry while we register the dataset on it. We first register the dataset of images $\{I_i\}_{i=1,\dots N}$ on the current reference image I^n_{mean} (the initial reference image I^0_{mean} is chosen among the dataset) according to the steps described at the beginning of this section. The resulting deformation fields T^n_i registering the initial images I_i to the current reference image I^n_{mean} are averaged. The inverse of this average deformation field T^n_{mean} is applied to the current reference image I^n_{mean} which then gets closer to a barycentric geometry of the dataset (see Fig. 1). Finally, the intensities are averaged in this new average geometry. Therefore through the deformation fields T^n_i, the original geometry and intensities of each heart are taken into account in the new average heart I^{n+1}_{mean}. One iteration can be summarized in the following equation:

$$I^{n+1}_{mean}(x) = \frac{1}{N}\sum_{i=1}^{N} I_i\Big(T^n_i \circ [T^n_{mean}]^{-1}(x)\Big)$$

where:
x is the voxel position,
I_i is the anatomical MRI of the sample i where $i = 1 \cdots N$ ($N = 9$ in our case),
I^n_{mean} is the current average anatomical MRI at the step n,
T^n_i is the deformation field matching the current average image I^n_{mean} to I_i,
$T^n_{mean} = \frac{1}{N}\sum_{i=1}^{N} T^n_i$ is the average deformation field at the step n.

These steps are repeated using the new average heart I^{n+1}_{mean} as the reference geometry until it converges. In practice, a few iterations are sufficient to get a stable geometry. Finally, the outputs of this process are an average geometry and intensities of the anatomical MRIs and a dense deformation field for each heart of the dataset.

Registration of the DT-MRIs: Since the anatomical MRIs and the DT-MRIs are co-acquired, we can apply directly the deformation fields obtained in the previous section to the DT-MRIs. We use the Log-Euclidean metric to interpolate diffusion tensors, and the *Finite Strain* (FS) reorientation strategy is preferred to the *Preservation of the Principal Direction* (PPD) [1] to transform the tensors. Indeed, the FS has the property to preserve the gradient of the diffusion tensor field and thus the transmural variations of the fibre and laminar sheet orientations known to be common features between hearts. Furthermore, this reorientation strategy is consistent with the similarity-invariant Log-Euclidean metric used afterwards. The statistics computed with the Log-Euclidean metric should not depend on the reference geometry which would not be the case with the PPD where the reorientation depends on the original tensor.

Statistics: The Log-Euclidean framework [2] provides a consistent and rigorous framework to study the statistical variability of diffusion tensors. Indeed,

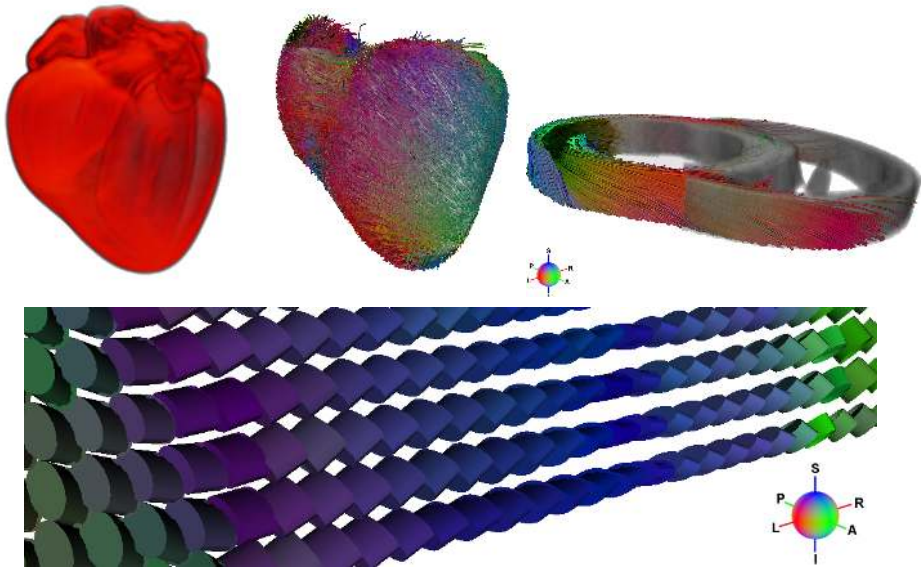

Fig. 2. [*Upper Left*] Average geometry of the canine hearts. [*Upper Middle*] Side view of fibre tracking computed on the average DT-MRI. [*Upper Right*] Fibre tracking on a few slices of the average DT-MRI to show the transmural variation of fibre orientation. [*Down*] Transmural variation of the laminar sheet orientation. Tensor visualization with cylinders. The base of the cylinder is the plane given by the primary and secondary eigenvectors. The height of the cylinder shows the laminar sheet orientation. The colors describe the orientation of the primary eigenvector according to the color sphere.

in this framework the space of diffusion tensors becomes a vector space where the statistics are consistent with the positivity constraint of the diffusion tensors. We compute the Log-Euclidean mean $\overline{D}_{log}$ of all the registered DT-MRIs $\{D_i\}_{i=1,\dots N}$ and the corresponding unbiased covariance matrix Cov of the whole diffusion tensors [15] at each voxel x of the average geometry:

$$\overline{D}_{log}(x) = \exp\left(\frac{1}{N}\sum_{i=1}^{N}\log\Big(D_i(x)\Big)\right)$$

$$Cov(x) = \frac{1}{N-1}\sum_{i=1}^{N} vec\Big(\Delta D_i(x)\Big).vec\Big(\Delta D_i(x)\Big)^t$$

where:

N is the size of the dataset,

$\Delta D_i(x) = \log\Big(D_i(x)\Big) - \log\Big(\overline{D}_{log}(x)\Big)$,

$vec(D) = (D_{11}, \sqrt{2}D_{12}, D_{22}, \sqrt{2}D_{31}, \sqrt{2}D_{32}, D_{33})^t$ is the minimal representation [15] of the diffusion tensor $D = (D_{ij})_{i,j=1,2,3}$

We project this covariance matrix of diffusion tensors along specific directions in the tangent plane at the mean diffusion tensor to extract the variances of the eigenvalues and eigenvectors orientations [16].

Resulting Statistical Atlas: We applied this framework to the dataset of 9 canine hearts presented previously in Section 2. We obtain an average geometry and a smooth cardiac DT-MRI atlas describing the whole cardiac fibre architecture: the fibre and laminar sheet orientations (see Fig. 2). The norm of the covariance matrix, homogeneous to a ratio, shows a global stability of the cardiac fibre architecture among the population of canine hearts (see Fig. 3). The average variability of the whole diffusion tensor is around 10%. A higher norm of the covariance matrix at the RV and LV endocardial apices and in the papillary muscles reveals regions where the fibre structure is probably not as much structured as the compact myocardium.

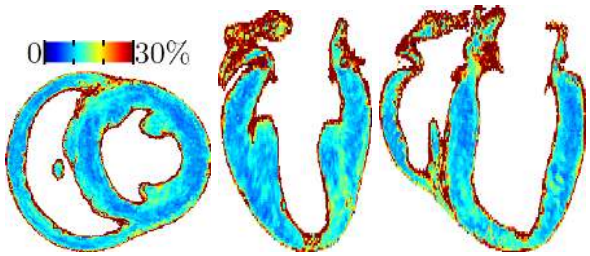

Fig. 3. Global variability $\sqrt{Tr(Cov)}$ (homogeneous to a ratio and expressed as a percentage) of the whole tensor in three different orthogonal views: a short axis and 2 long axis views.

4 Comparisons of Cardiac Fibre Architectures

4.1 Comparison Measures

Any given new dataset can be registered with the atlas using the presented methodology. Then we perform the comparison using different measures:

- the normalized Mahalanobis distance $\tilde{\mu}$ to the atlas at each voxel, given by the formula [15]: $\tilde{\mu}^2(\overline{D}_{log}, D_{heart}) = \frac{1}{d} vec(\Delta D)^t . Cov^{-1} . vec(\Delta D)$ where $d = 6$ is the dimension of the diffusion tensors space.
- the spatial distribution of the angular difference of the primary eigenvector (see Fig. 5).
- the histograms of the angular difference of the eigenvectors with the atlas, for a qualitative statistical comparison (see Fig. 6, left column).
- the histograms of the Mahalanobis distance of the eigenvectors orientation to the atlas, for a quantitative statistical comparison (see Fig. 6, right column). This gives the angular differences of the eigenvectors normalized by the variance of the statistical atlas at each voxel. Thus, we measure the difference of the eigenvectors orientation according to its dispersion among the population used to build the atlas.

A synthetic view of the comparison of the histograms is then given by the mode of the distributions (see Table 1).

4.2 Atlas Comparisons with a Human Heart and a Synthetic Model

We proceed to a limited inter-species comparison of the fibre architecture between human and canine hearts. Indeed, the difficulty to obtain normal human hearts for research purpose (normal hearts are preferably used for transplantation) is the main obstacle to the building of a human atlas. In our case, only one human heart is available in the JHU database, and the quality of this heart is lower than that of canine DT-MRIs. The mode of the normalized Mahalanobis distance is 1.49 whereas it is lower than 1 for canine hearts of the dataset. Most of the important differences are located in the right ventricular wall and part of the septum. In Fig. 6 and Table 1, we observe that the fibre orientation of the human heart is closer to the canine population than its laminar sheet orientation.

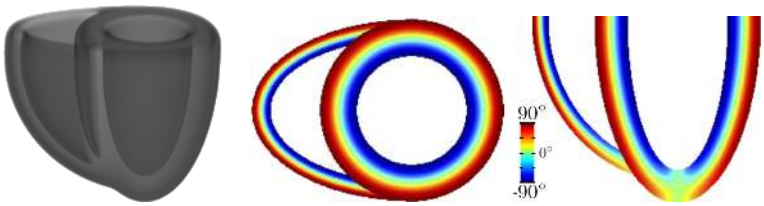

Fig. 4. [*Left*] Geometry of the synthetic model. [*Middle and Right*] Elevation angle of the synthetic fibre orientation in short axis and long axis views (from Sermesant *et al.* [21]).

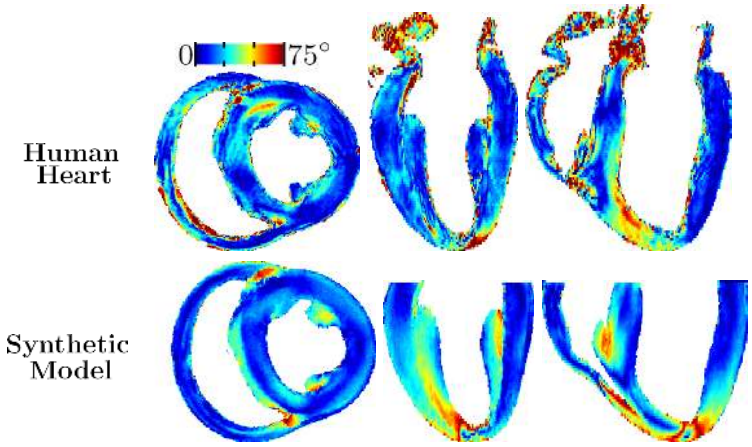

Fig. 5. [*Up*] Angle between the primary eigenvector of the atlas and the human heart. [*Down*] Angle between the primary eigenvector of the atlas and the fibre orientation of the synthetic model. (one short axis and two long axis views).

The synthetic model proposed in [21] describes the fibre orientation in an ellipsoidal template geometry of the ventricles(see Fig. 4). The orientation difference of the primary eigenvector of the atlas and the fibre orientation of the synthetic model has a mode of 19.6 degrees while the mode for the canine hearts is 6.9 degrees, and respectively 0.95 and 0.58 for the mode of its Mahalanobis

distance (see Fig. 6 and Table 1). The synthetic model is clearly different from the population of canine hearts. For instance, we observe in the short axis view a modeling problem at the crossing of the two ventricular walls. Indeed, the synthetic model has an important discontinuity in this region. Furthermore, the synthetic approach reaches its limits at the right ventricular and left ventricular apices (see Fig. 5) where the fibre organization modeling probably needs different analytical laws from the compact myocardium. The ellipsoidal geometry and the fibre orientation of the synthetic model are too simple to be realistic in catching all the subtle variations of the fibre orientation.

Eigenvector/Heart	Canine Hearts	Human Heart	Synthetic Model
Primary	6.9° - 58%	10.1° - 81%	19.6° - 95%
Secondary	11.6° - 57%	36.2° - 115%	-
Tertiary	11.4° - 46%	29.1° - 109%	-

Table 1. Modes of the distributions of the angular differences of the eigenvectors and their Mahalanobis distances (respectively in degrees and % of the variance).

5 Conclusion and Perspectives

We presented here a framework for building a statistical atlas of cardiac fibre architecture in an average geometry. This statistical framework can be extended to comparison between specimen or species. The resulting atlas has been compared to a human heart and a synthetic model of the fibre orientation. In the case of the human heart, we observed more differences on the laminar sheet orientation than on the fibre orientation. The synthetic model seems to need some improvements for a better description of the fibre organization, especially adding an accurate description of the laminar sheet orientation. Having access to canine and human heart databases of greater size should help in improving the relevance of the statistical atlas and the inter-species comparisons. The effects of these differences on the electromechanical behavior still remain to be studied for a complete evaluation of the relevance to use such atlases in patient-specific clinical applications.

Acknowledgment

This research was funded by Siemens Corporate Research, Princeton, NJ. Acquisition of the DT-MRIs data was funded by the Intramural Research Program of the National Heart Lung and Blood Institute (E.R. McVeigh Z01-HL4004609). We thank Drs. Patrick A. Helm and Raimond L. Winslow at the Center for Cardiovascular Bioinformatics and Modeling for provision of data, P. Fillard and N. Toussaint for provision of diffusion tensors and fibre tracking computation and visualization tools[6].

[6] http://www-sop.inria.fr/asclepios/software/MedINRIA/

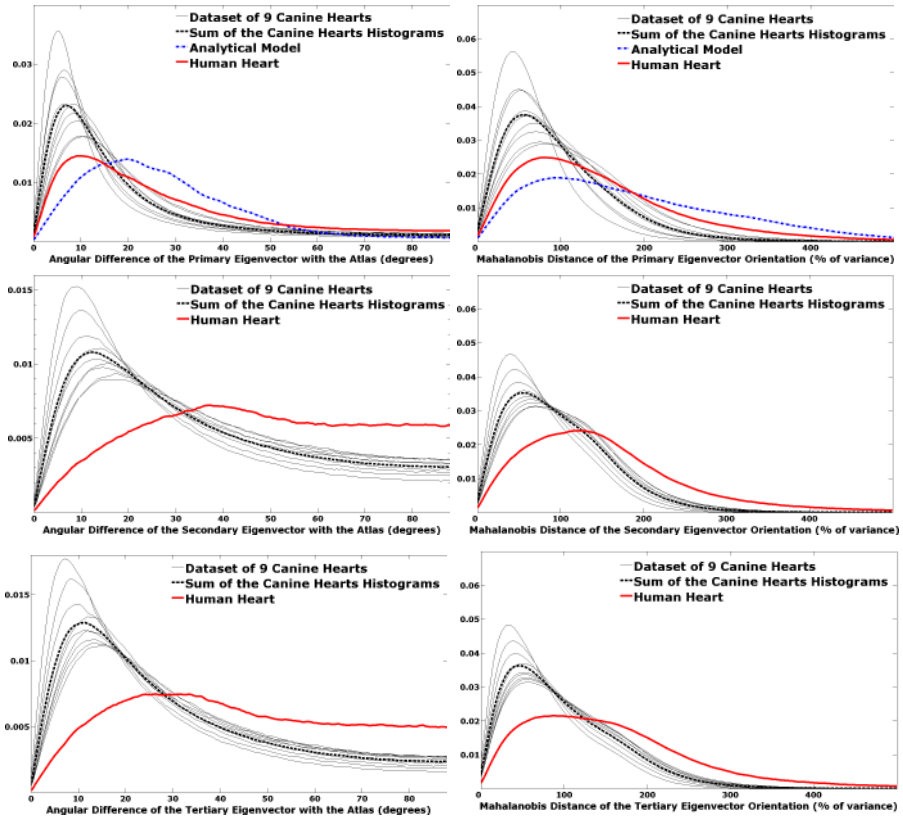

Fig. 6. [*Left Column*] Normalized histograms of the primary, secondary and tertiary eigenvectors variations around their mean. [*Right Column*] Mahalanobis distance of the primary, secondary and tertiary eigenvectors variations around their mean.

References

1. D.C. Alexander, C. Pierpaoli, P.J. Basser, and J.C. Gee. Spatial Transformations of Diffusion Tensor Magnetic Resonance Images. *IEEE TMI*, 20(11):1131–1139, 2001.
2. V. Arsigny, P. Fillard, X. Pennec, and N. Ayache. Fast and Simple Calculus on Tensors in the Log-Euclidean Framework. In *Proc. of MICCAI'05*, volume LNCS 3749, pages 115–122, 2005.
3. T. Arts, K.D. Costa, J.W. Covell, and A.D. McCulloch. Relating Myocardial Laminar Architecture to Shear Strain and Muscle Fiber Orientation. *Am J Physiol Heart Circ Physiol*, 280:H2222–H2229, 2001.
4. N. Ayache, editor. *Computational Models for the Human Body*. Handbook of Numerical Analysis. Elsevier, 2004.
5. A. Azar, C. Xu, X. Pennec, and N. Ayache. An interactive Intensity- and Feature-Based Non-Rigid Registration Framework for 3D Medical Images. In *Proc. of ISBI'06*, 2006.
6. C. Chefd'hotel, G. Hermosillo, and O. Faugeras. Flows of diffeomorphisms for multimodal image registration. In *Proc. of ISBI'02*, 2002.

7. K.D. Costa, J.W. Holmes, and A.D. McCulloch. Modelling cardiac mechanical properties in three dimensions. *Philosophical Transactions of the Royal Society A: Mathematical, Physical and Engineering Sciences*, 359(1783):1233–1250, 2001.
8. J. Dou, T.G. Reese, W.I. Tseng, and J. Van Wedeen. Cardiac diffusion MRI without motion effects. *Magnetic Resonance in Medecine*, 48(1):105–114, 2002.
9. A. Guimond, J. Meunier, and J.-P. Thirion. Average brain models: A convergence study. Technical Report 3731, INRIA, Sophia-Antipolis, France, July 1999.
10. P. Helm, M. Faisal Beg, M.I. Miller, and R.L. Winslow. Measuring and mapping cardiac fiber and laminar architecture using diffusion tensor MR imaging. *Ann N Y Acad Sci*, 1047:296–307, 2005.
11. P.A. Helm, H.J. Tseng, L .Younes, E.R. McVeigh, and R.L. Winslow. Ex Vivo 3D Diffusion Tensor Imaging and Quantification of Cardiac Laminar Structure. *Magn. Reson. Med.*, 54(4):850–859, 2005.
12. P.J. Hunter, A.J. Pullan, and B.H. Smaill. Modeling Total Heart Function. *Annu Rev Biomed Eng.*, 5:147–177, 2003.
13. I.J. LeGrice, B.H. Smaill, L.Z. Chai, S.G. Edgar, J.B. Gavin, and P.J. Hunter. Laminar structure of the heart: ventricular myocyte arrangement and connective tissue architecture in the dog. *Am J Physiol Heart Circ Physiol*, 1995.
14. I.J. LeGrice, Y. Takayama, and J.W. Covell. Transverse Shear Along Myocardial Cleavage Planes Provides a Mechanism for Normal Systolic Wall Thickening. *Am J Physiol Heart Circ Physiol*, 1995;77:182-193.
15. X. Pennec, P. Fillard, and N. Ayache. A Riemannian Framework for Tensor Computing. *International Journal of Computer Vision*, 2006.
16. J.-M. Peyrat, M. Sermesant, X. Pennec, H. Delingette, C. Xu, E. McVeigh, and N. Ayache. Towards a Statistical Atlas of Cardiac Fiber Architecture. Research Report 5906, INRIA, May 2006.
17. J.-M. Peyrat, M. Sermesant, X. Pennec, H. Delingette, C. Xu, E. McVeigh, and N. Ayache. Towards a Statistical Atlas of Cardiac Fiber Structure. In *Proc. of MICCAI'06*, volume LNCS 3749, pages 115–122, 2006.
18. F. Sachse, editor. *Computational Cardiology - Modeling of Anatomy, Electrophysiology, and Mechanics*. Lecture Notes in Computer Science. Springer, 2004.
19. D.F. Scollan, A. Holmes, R.L. Winslow, and J. Forder. Histological validation of myocardial microstructure obtained from diffusion tensor magnetic resonance imaging. *Am J Physiol Heart Circ Physiol*, 275:H2308–H2318, 1998.
20. M. Sermesant, H. Delingette, and N. Ayache. An electromechanical model of the heart for image analysis and simulation. *IEEE TMI*, 25(5):612–625, 2006.
21. M. Sermesant, K. Rhode, G.I. Sanchez-Ortiz, O. Camara, R. Andriantsimiavona, S. Hegde, D. Rueckert, P. Lambiase, C. Bucknall, E. Rosenthal, H. Delingette, D.L. Hill, N. Ayache, and R. Razavi. Simulation of cardiac pathologies using an electromechanical biventricular model and XMR interventional imaging. *Med. Image Anal.*, 5(9):467–80, October 2005.
22. D. Streeter and C. Ramon. Muscle pathway geometry in the heart wall. *J Biomechanical Engineering*, 105:367373, 1983.
23. H. Sundar, D. Shen, G. Biros, H. Litt, and C. Davatzikos. Estimating Myocardial Fiber Orientation by Template Warping. In *Proc. of ISBI'06*, 2006.
24. T.P. Usyk, R. Mazhari, and A.D. McCulloch. Effect of Laminar Orthotropic Myofiber Architecture on Regional Stress and Strain in the Canine Left Ventricle. *Journal of Elasticity*, 61:143–164, 2000.